Cyclic elastoplastic behaviour of 2198-T8 aluminium alloy welded panels

Xavier Truant, Georges Cailletaud, Florent Fournier Dit Chabert, Ivan Guillot, Serge Kruch

Cyclic elastoplastic behaviour of 2198-T8 aluminium alloy welded panels

Xavier TRUANT, Georges CAILLETAUD**, Florent FOURNIER DIT CHABERT***,*
*Ivan GUILLOT****, Serge KRUCH******
** CEA / Cadarache, TechnicAtome, Route de Vinon/Verdon, 13115 Saint Paul lez Durance, France*
*** Centre des Matériaux, MINES ParisTech, CNRS UMR 7633, 10 rue Henri Desbruères, B.P. 87, 91003 Evry Cedex, France*
****IRT Jules Verne, Chemin du Chaffault, 44340 Bouguenais, France*
***** Univ Paris Est Creteil, CNRS, ICMPE, UMR 7182, 2 rue Henri Dunant, 94320 Thiais, France*
****** DMAS, ONERA, Univ Paris Saclay, F-92322 Châtillon, France*
(corresponding author:serge.kruch@onera.fr, ORSID id: 0000-0003-2791-354X)

Abstract The Friction Stir Welding (FSW) process generally induces a gradient of properties and a softer behaviour along the welded joint. To design aeronautical structures welded by FSW in fatigue, it is necessary to study the impact of this localized soft behaviour on the overall structure. In this study, the 2198-T8 hardening structural aluminium alloy is considered. Monotonic and cyclic mechanical tests are performed by combining conventional extensometric measurements with digital image correlation (DIC) to measure the local displacement fields around the welded zone. Based on these experimental data, constitutive equations are proposed and identified, zone by zone, across the welded joint. In parallel, a quantification of T1 (Al_2CuLi) strengthening precipitates is performed in different regions of the joint with a transmission electron microscope in order to identify a relationship between the microstructure and the mechanical parameters. Finally, once all the material parameters are identified, the model is validated by a 3D finite element analysis representative of FSW samples.

Keywords

Al_2CuLi alloy, 2198-T8, Friction Stir Welding, Mechanical gradient behaviour, Digital Image Correlation, Cyclic plasticity

Declarations

Funding: This research was supported integrally by Onera (Office National d'Etudes et de Recherches Aérospatiales)

Conflicts of interest/Competing interests: Not applicable

Availability of data and material: The datasets generated during the current study are not publicly available due to legal restrictions.

Code availability (software application or custom code): Numerical analysis was performed with the Finite Element suite Zset developed by Ecole des Mines and Onera: http://www.zset-software.com

1. Introduction

The FSW process was developed in 1991 by the Welding Institute [1]. FSW is a solid-state process without any filler material. The temperatures reached are below the melting temperature of the material. This makes it possible to weld hard weldable materials such as aluminium alloys of the 2XXX series [2]. Today, it is used for airframes as an alternative to the riveting process. The third generation aluminium alloy 2198-T8 is considered in this

study. The addition of lithium improves the mechanical properties compared to 2024 [3] and reduces the weight of the structures. FSW welded samples have been tested under tensile mechanical loads in different studies [4, 5, 6, 7, 8 and 9]. Several approaches to determine the mechanical behaviour of a welded joint are proposed. One expensive and time-consuming approach is to mechanically test each zone using micro-samples cut across the joint [10]. Another approach, adopted and developed in this study, proposes to take advantage of all the sophisticated features of the digital image correlation technique which allows the observation of the displacement field in different regions of the joint [4, 5, 7, 8 and 9].

Generally, experimental data are used to propose and identify constitutive equations to reproduce the mechanical behaviour observed on a 2198-T8 welded joint from simple tensile tests as in the work of Le Jolu [4]. Here, we focus our analysis on the low cycle fatigue behaviour of welded joints which requires an additional degree of complexity in the modelling. It is recalled that a correct consideration of the cyclic behaviour of the material is a fundamental preliminary step in the modelling of fatigue crack initiation. However, this last point is not addressed in this paper.

The observation of the microstructure of the base metal (BM) 2198-T8 allowed the quantification of T1 precipitates (Al_2CuLi) with a transmission electron microscope [11]. The evolution of the T1 reinforcement precipitates is observed by Cavaliere [12] in different areas of a 2198-T8 welded joint. An evolution of the number, shape and distribution of these precipitates is observed over the whole joint. In the work of Gao [13], this precipitation is also quantified for a welded joint in 2198-T8. A link between the yield strength of each zone of the joint and the resistance mechanisms, involved by precipitates or T1 dislocations, is proposed.

The paper is divided in the following sections. First, experimental procedures are extensively described regarding the analysis of the microstructures along the welded joint as well as the mechanical tests and their instrumentations especially developed for these tests. Based on these experimental results, section 3 presents the mechanical model proposed to simulate as accurately as possible the cyclic behaviour of the welded joint

2. Experimental procedures and results

2.1 Welding Al-Cu-Li 2198-T8 samples

The 2198-T8 aluminium alloy under consideration is described in Table 1.

Elements	Al	Cu	Li	Ag	Mg	Zr	Fe	Si	Zn	Ti
wt%	Bal.	3.2	0.97	0.32	0.31	0.11	0.04	0.03	0.02	0.02

Table 1 2198-T8 aluminium alloy composition in wt%

The welding process is carried out at ONERA with a POWERSTIR 25T device from Crawford Swift Ltd, with a speed feed of 0.4. The tool used [14] has a shoulder diameter of 13 mm and a pin diameter of 4.2 mm. The length of the pin is adjusted to be less than the thickness of the sheet which is about 3.18 mm. Welding is mainly carried out in the longitudinal direction of rolling, called L. However, since aluminium 2198-T8 is known to be highly anisotropic, welding is also carried out in the other two main rolling directions (called T for the transverse direction and D for the 45° direction). It is very important to study the effect of the welding direction in relation to the rolling direction of the sheet on the mechanical properties of the welded joints.

Regarding the width of the specimen affected by the welding process, it is possible to distinguish 4 zones each with a specific microstructure. From the left to right on the top of figure 1 (with a symmetry with respect to the centre of the welded zone), the base metal (BM) is the zone where the microstructure is not affected by the process. In the Thermal Affected Zone (TAZ), the microstructure is only influenced by the temperature. In the Thermo-Mechanical Affected Zone (TMAZ) an influence of temperature is observed as well as an important rotation of the microstructure. Finally, the Nugget Zone (NZ) is characterized by a completely recrystallized microstructure.

2.2 Microhardness analysis

Microhardness is measured through the welded joint with a Buehler device (Omnimet MHT 5101) and a 100g load. Measurements are taken halfway through the thickness of the sheet.

The evolution of the microhardness along the welded width, presented on figure 1, shows a maximum hardness in the base metal, away from the centre of the joint, of about 160 HV0.2. An important gradient is observed in the TAZ and TMAZ zones. Finally, the minimum hardness occurs in the nugget zone with a value of about 120 HV0.2. In order to describe more accurately this strong gradient the TAZ and TMAZ are divided in two parts. Based

on these observations, the welded joint will be then characterized by 6 regions: BM, TAZ2, TAZ1, TMAZ2, TMAZ1 and NZ from the left to the right. To be more precise it is also convenient to distinguish the left hand side (advancing side) and the right hand side (retreating side), from the centre of the NZ, where the microstructure of the Thermo-Mechanically Affected zones may vary because of the rotation direction of the pin. However, from these first observations and the microhardness analysis, it is not possible to distinguish an influence of the rotation direction from both retreating and advancing sides

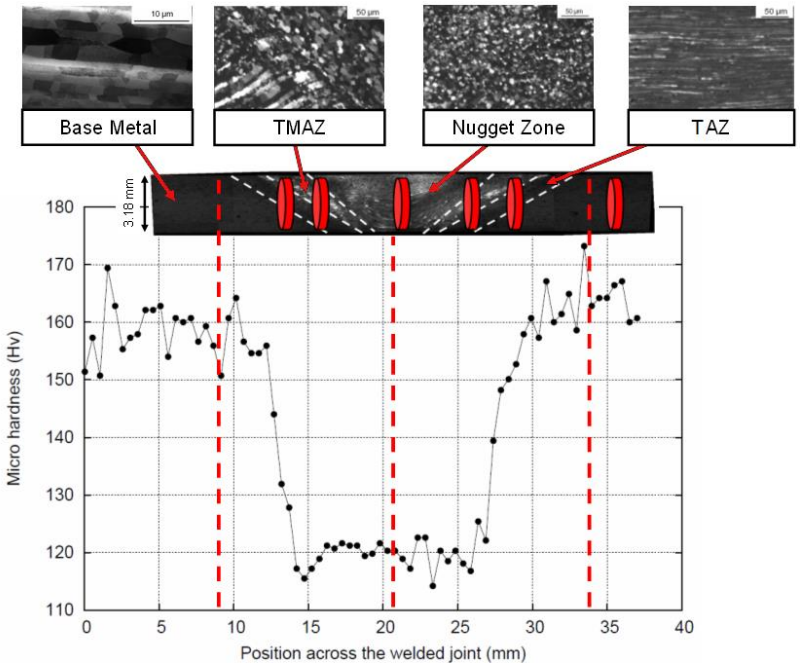

Fig 1 Micro hardness through the welded joint and the thin foils taken in different region of the joint

2.3 Microstructure quantification

Transmission electron microscopy (TEM) analyses were performed on 3 mm diameter and 750 µm disks were cut from different areas of the welded joint (figure 1). The slices were thinned down to about 100 µm by mechanical polishing and finally thinned by the classical twin-jet electropolishing apparatus with solution of nitric acid (1/3) in methanol (2/3) at -30 °C using a 12V tension. Microstructures are observed by transmission electron microscopy at 200kV with a JEOL 2000EX.

The three main precipitations most commonly observed on a very fine scale in the 2198 aluminium alloy in the T8 state are: δ'-Al3Li, θ'-Al2Cu and T1-Al2CuLi. The T1 precipitates that form very thin platelets of high aspect ratio on the {111} planes of the aluminium matrix are considered to play a key role in the strengthening of aged commercial Al-Cu-Li alloys [15-22]. These T1 precipitates are roughly homogeneously distributed in the matrix and were easily imaged by conventional dark field TEM in different regions of the welded joint in order to be able to quantify them. The length and thickness of the T1 precipitates were measured from dark-field TEM micrographs of the particles viewed edge-on by selection of one diffuse streak corresponding to a $(0002)_{T1}$ reflection parallel to the diffraction vector (111) of the aluminium matrix (Figure 1). The difficulty is to separate some precipitates that are too close, so the Fiji software [23] is used to extract the length as accurately as possible. The measurements were performed on ten dark field images from different grains of the thin foil, the values obtained correspond at least to the average of 1000 precipitates. For the base metal, i.e. far from the weld zone, the mean length of the precipitates T1 is 58±25 nm and the thickness 3.5±1.2 nm.

The values of the lengths and thicknesses of precipitate T1 measured in the thermal-affected zone 2 (TAZ2) are the same as in the BM (Figure 2.b), however the volume fraction decreases from 6.9% in the BM to 5.0% in TAZ2. In the TAZ1 zone, near the weld joint nugget, the photograph in Figure 2.C. shows that the number of T1 precipitates is much lower and that the microstructure is changing to smaller and thicker precipitates than in the BM.

It is then measured to be about 48.6 nm long and about 4.7 nm thick at a volume fraction of 2.7%. Precipitation is not quantified in TMAZ.

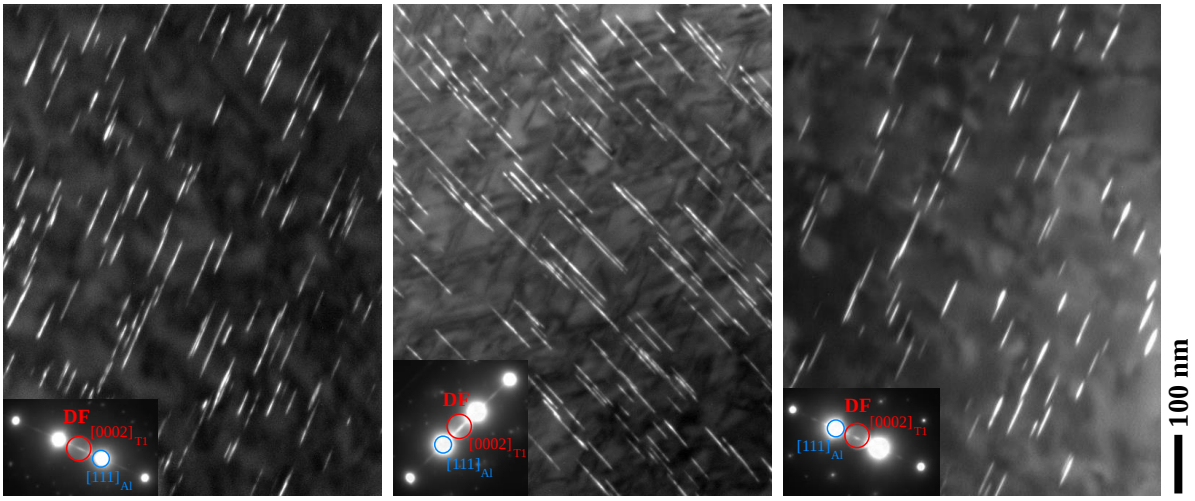

Fig 2 T1 precipitation, (a.) Base Metal (BM), (b.) Thermal Affected Zone 2 (TAZ2) and (c.) Thermal Affected Zone 1 (TAZ1)

Figure 3a shows a dark field of T1 precipitates as seen from above, which are almost hexagonal in shape. Figure 3b, which corresponds to a weak beam of the aluminium matrix in the same area, shows curved dislocations pinned on T1 precipitates. The precipitates are therefore bypassed by the dislocations and shear of these precipitates was not observed. The Nugget Zone (NZ) is characterized by total dissolution of the T1 precipitates in this zone, and there are only few helical dislocations (Figure 4) that originate from the precipitation on dislocations of vacancies formed at high temperature during welding.

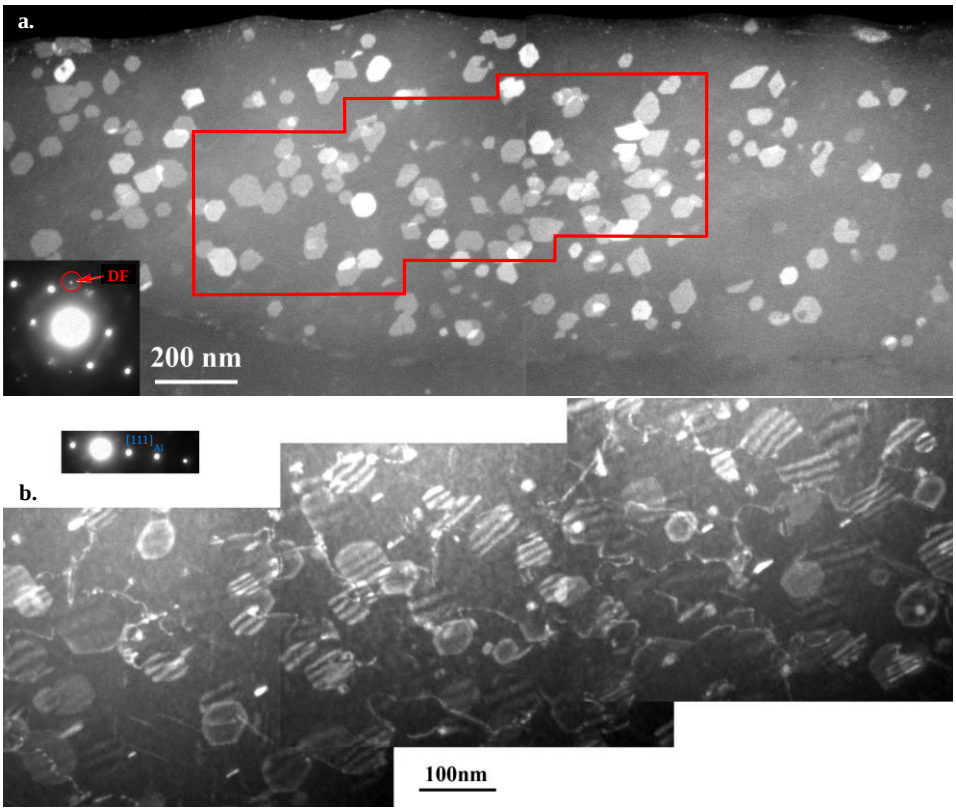

Fig 3 T1 precipitation in TAZ. (a.) dark field of T1 precipitates as seen from above, and (b.) [111] weak beam of the aluminium matrix.

However, the thickness of the precipitates measured in TEM is only approximate as a result of the variation in the illumination of the precipitates in a dark field due to the presence of internal stresses in the thin foil. The results obtained in SAXS in the work of Decreus [24] show a thickness of these precipitates of about 1.3 nm and a volume fraction of about 5.2% for the base metal. Consequently, the volume fraction, length and thickness of the precipitates are re-evaluated in the TAZ1 and TAZ2 zones in relation to the base metal data obtained in [24]. The values are presented in Table 2.

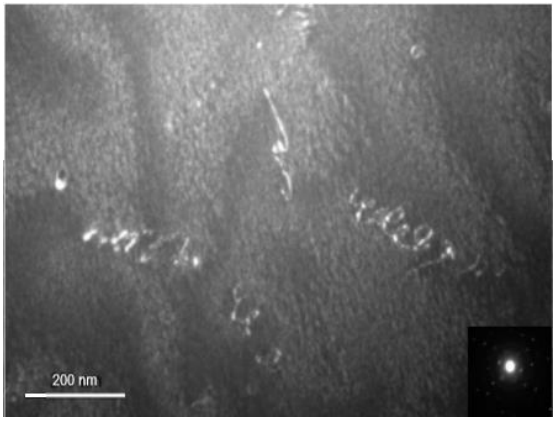

Figure 4: weak beam of the aluminium matrix, total dissolution of the T1 precipitation into the Nugget Zone (NZ)

	Base Metal	TAZ2 A	TAZ1 A	Nugget Zone	TAZ1 R	TAZ2 R
Volume Fraction fv	0.052	0.037	0.020	0.	0.017	0.034

Table 2 Microstructure parameters in different zones of the joint (A and R refers to Advancing and Retreating sides respectively)

The density of dislocations is taken into account in this study thanks to the results of Gao [13]. Using X-ray diffraction and the Williamson-Hall method [25], a dislocation density of 2.1×10^{14} m^{-2} and 10.1×10^{14} m^{-2} can be measured in the nugget zone and in the base metal, respectively. Subsequently, these values will be used to determine a yield strength contribution in different areas of the welded joint.

2.4 Mechanical tests

The monotonic and cyclic tensile tests are performed at room temperature on a 100 kN LOS SYSTEM servohydraulic device from Losenhausen (Great Britain) Ltd. The cyclic tests are carried out on the same installation with a symmetrical load ratio (R = -1, stress controlled). An anti-buckling device has been designed as proposed by Khan et al. [26]. Effects of this device are not negligible and will be discussed below. For each sample, 4 successive load levels were tested (Figure 5). The base metal and welded joints were tested using either stress or strain control.

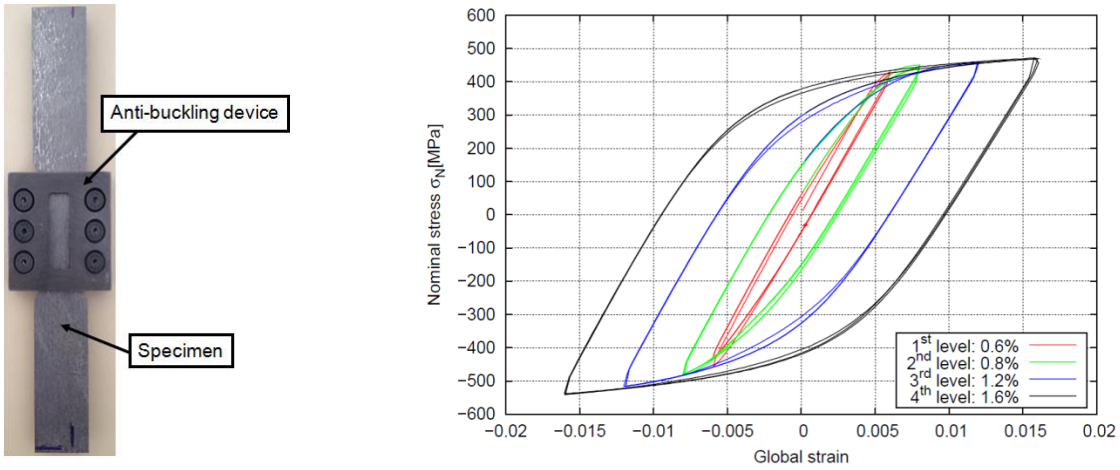

Fig 5 Anti-buckling device and the base metal specimen (left), overall mechanical behaviour of the base metal for symmetric loadings and four different strain levels (right)

For the welded specimens, digital image correlation (DIC) is used to measure the displacement fields, to calculate the total strains and thus to be able to obtain local stress-strain curves. This technique has already been used on inhomogeneous materials [7]. During the mechanical tests, images are taken with an Aramis 4M, CMOS, Titanar 5.6/100 camera (resolution 2352x1728 pixels). The grey level contrast is obtained by using a pattern of speckle marks on the surface of the sample, consisting of black and white spots. The ARAMIS [27] software is used to analyse the images, to measure the displacement fields and to calculate the strain fields. For DIC, subsets of 35x35 pixel images are chosen, which corresponds to an area of 0.6x0.6 mm2. Such a size of subsets is well suited to capture the gradient of mechanical properties across the welded joint with a fairly good accuracy.

3. Model identification

3.1 Experimental results

Figure 6 shows the resulting strain fields taken at two different times during the tensile test. Figure 7 plots the evolution of the longitudinal displacement and strain as a function of the position along the weld ligament, at different times. At the beginning of the tensile test, the displacement curve is linear across the weld joint. The experimental displacement data are evenly spaced and the deformation is homogeneous within the specimen. At the end of the tensile test, the shape of the displacement curve describes a sigmoidal curve. The displacement contours are no longer uniformly spaced. The strain in the region inside and near the weld varies from about 0.4 % outside the shoulder diameter to about 30 % in the centre of the nugget. The weld creates a strong inhomogeneity in the material properties and most of the plastic deformation is concentrated in the region of the weld. In summary, strains are localized in the weakest area of the sample which is, in our case, the centreline of the weld (Fig. 6, right). The stress-strain response evaluated by the local DIC at the centre of the weld shows a high level of plasticity while the base metal remains mainly elastic. DIC results make it possible to directly extract the constitutive stress-strain behaviour for each region of the welded joint.

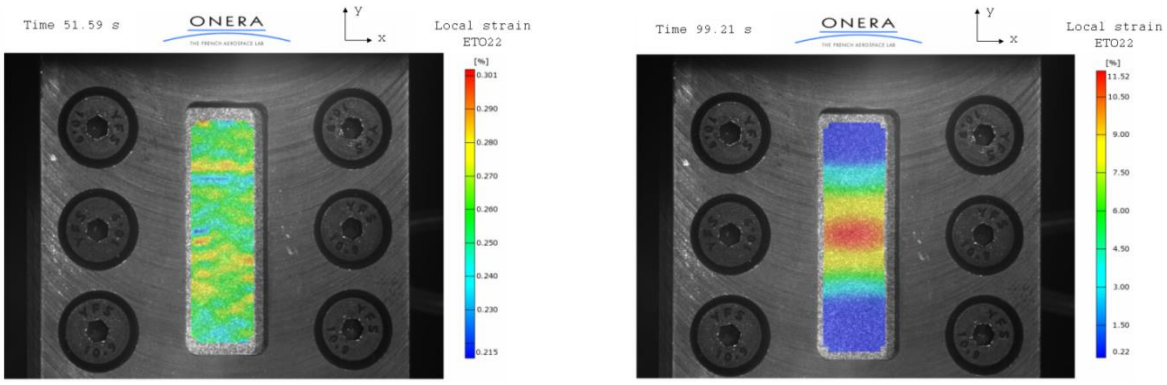

Fig 6 Results of strain fields at two different times (50 s and 98 s) during the tensile test

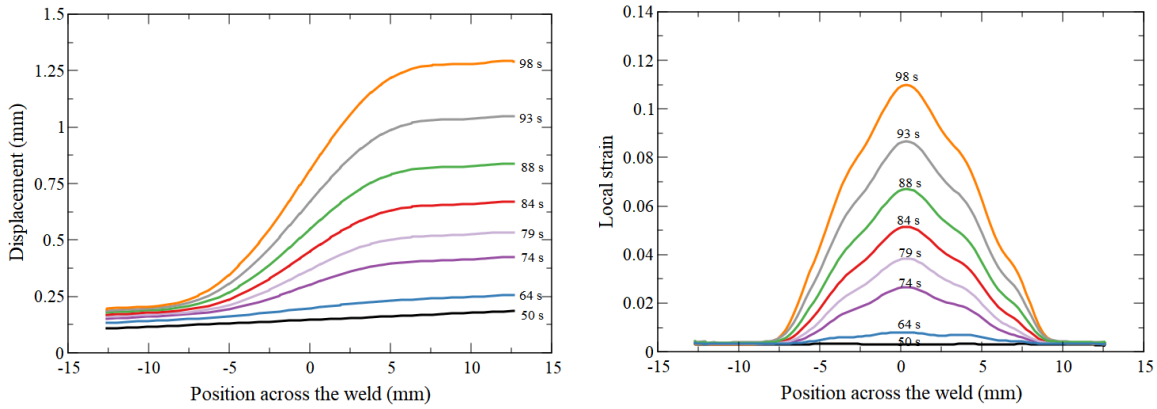

Fig 7 Evolution of the displacement (left) and the strain (right) as a function of the position along the weld for eight loading times

A first validation of these measurements consists in comparing an average of the local strains with the values recorded using a conventional extensometer (Figure 8a). Due to the fact that the local stress is not uniform and not measurable, it was decided to use the mean stress on the ligament (i.e. the force divided by the effective cross-section of the specimen) in order to be able to relate it to an experimental measurement. Despite the high strain levels that can be reached in the single tension tests, the strain plotted in all the figures of this paper is the engineering strain as it is explained in the next section of the paper.

The good correlation between the two measurements techniques (DIC and conventional) allows to validate the measurement of displacements and the calculation of the strain. Then the local strain values can be evaluated in other regions from the centre line of the joint (red curve in figure 8b) to the base metal (black curve in figure 8b). As seen previously, the centre of the welded joint exhibits a high level of plasticity while the base metal remains practically elastic. For the constitutive behaviour, the weld appears to have a lower yield strength and also a lower hardening modulus than the base metal.

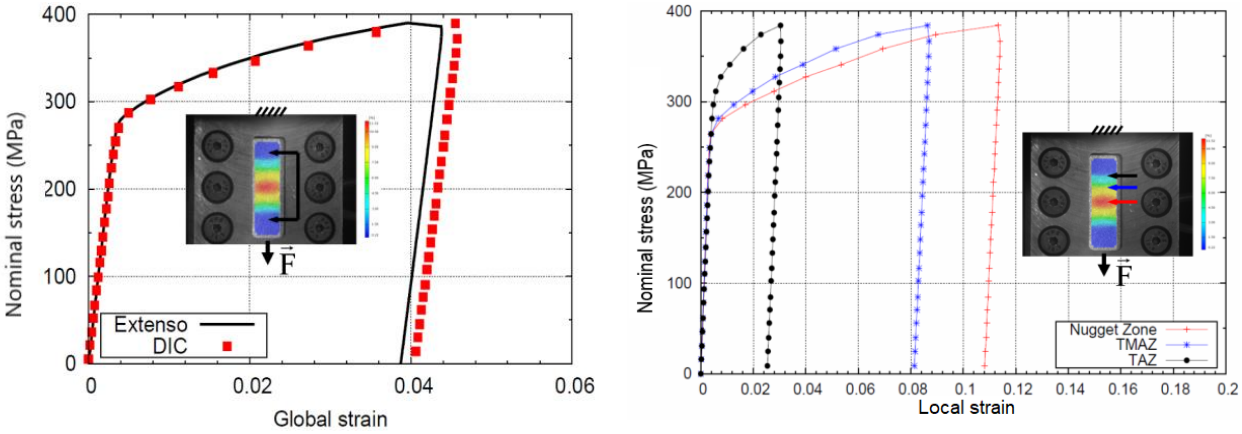

Fig 8 a) Comparison between the DIC assessed strain values and those obtained by the conventional technique, b) Assessment of the local strain values at 3 different regions of the welded joint

The experimental device being in place, cyclic tests are performed to characterize the local cyclic mechanical behaviour along the welded joint. The sample is loaded with several increasing cyclic loads, for instance 30 cycles at 300 MPa (global load), 20 cycles at 320 MPa, 10 cycles at 340 MPa and 5 cycles at 360 MPa.
Figure 9 (left) shows the stress-strain behaviour of the nugget zone, taken directly from the DIC results. Again, the stress is assumed to be the value of the continuous engineering stress in each section of the specimen. For each stress level, only the first hysteresis loop is plotted for sake of clarity. As observed previously, the nugget area shows a high level of plasticity. Significant isotropic hardening is also observed in each zone of the welded joint. The evolution of the total plasticity range as a function of the number of cycles is presented in figure 9 (right). The nugget zone shows a greater isotropic hardening than the other regions. For the highest levels, it can be seen that the number of cycles performed is not sufficient to reach a stabilized hysteresis loop. These results will be improved with longer cyclic tests.

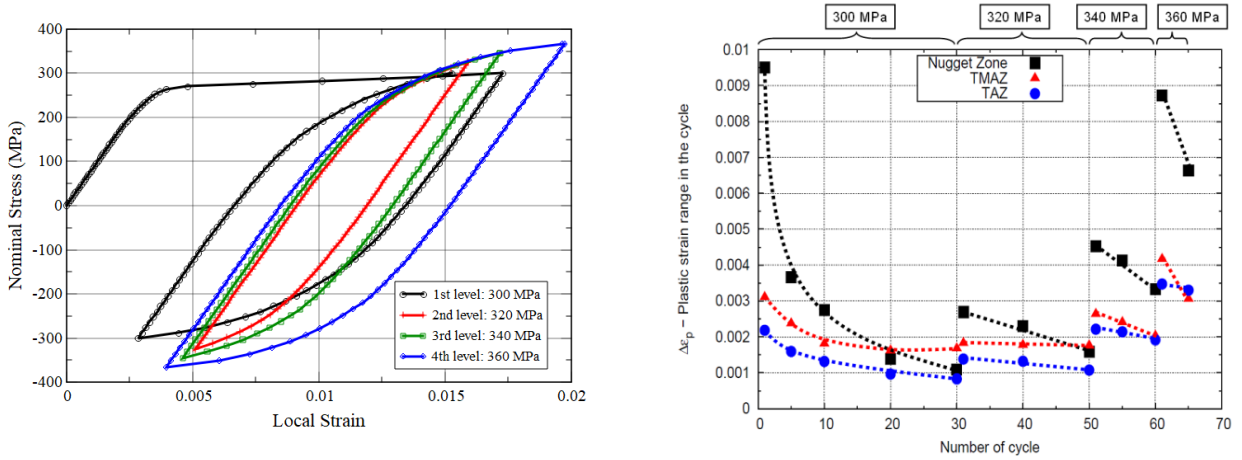

Fig 9 Local behaviour of the nugget zone obtained with DIC for symmetrical loads (left) and observation of cyclic hardening for three different zones in the welded joint and for four stress levels (right)

These results validate the DIC technique to evaluate the stress-strain constitutive behaviour directly extracted from the different regions of the experimental sample. In particular, kinematic and isotropic hardenings can be clearly identified. However, the strain range over which the constitutive behaviour of a particular region of the weld is measured, is limited by the strength of the weakest area of the weld microstructure. Tensile test results show that, just prior to the specimen failure, the base metal remains almost elastic while the weld centreline has a high level of plasticity. Therefore, the evaluation of the cyclic constitutive behaviour of the base metal should be carried out on homogeneous samples without welds.

3.2 Mechanical behaviour modelling

The aluminium sheet is highly anisotropic due to the rolling manufacturing process [28]. Nevertheless, since we are considering, for the moment, samples with a welding direction in the rolling direction L, we decide to use, as a first approximation, an isotropic elastoplastic Chaboche's model using a Von Mises criterion [29, 30, 31]. Equations are briefly presented below (bold symbols represent second order tensors).

The plastic criterion writes:

$$J(\boldsymbol{\sigma}) = \sqrt{\frac{3}{2}\,(\boldsymbol{\sigma}' - \boldsymbol{X}) : (\boldsymbol{\sigma}' - \boldsymbol{X})} - R_0 - R$$

where $\boldsymbol{\sigma}'$ represents the deviatoric part of the stress tensor.

The plastic potential is characterized by a plastic threshold R_0, 2 isotropic nonlinear hardenings of Voce type, *Ri*, and 3 terms of nonlinear kinematic hardening of Armstrong-Frederick type with backstresses ***Xj*** (there is no summation on repeated indices).

$$\boldsymbol{X}_j = \frac{2}{3}\,C_j\,\boldsymbol{\alpha}_j \quad \text{with} \quad d\boldsymbol{\alpha}_j = d\boldsymbol{\epsilon}^p - D_j\,\boldsymbol{\alpha}_j\,dp \quad j = 1,2,3$$
$$dR_i = b_i\,(Q_i - R_i)\,dp \quad i = 1,2$$

C_j, D_i, Q_i and b_i are material parameters to be identified, p is the cumulative plastic strain.

Table 3 summarizes the results of the identification of these material parameters for the different areas of the welded joint as defined in section 2. Areas are chosen in order to reproduce as precisely as possible the gradient of the mechanical behaviour experimentally observed.

The mechanical parameters are identified on a volume element, considering the local strains and the nominal stress. All the numerical developments have been implemented in the Finite Element suite Zset developed by Ecole des Mines and Onera.

The results are presented and discussed in the next section with a finite element analysis on a 3D meshed sample.

Zone in the joint	Young Modul.	Plasticity threshold	Non Linear Isotropic Hardening 1		NLIH 2		Non Linear Kinematic Hardening 1		NLKH 2		NLKH 3	
	E (GPa)	R_0 (MPa)	b1	Q1 (MPa)	b2	Q2	C1 (GPa)	D1	C2	D2	C3	D3
Base Metal	81	340	400	-80	30	0	378	4500	50	450	1	30
TAZ 2	81	340	400	-80	30	0	378	4500	50	450	1	30
TAZ 1	81	200	400	-80	30	120	378	4500	50	450	0.4	30
TMAZ 2	81	180	400	-80	30	120	378	4500	50	450	0.4	30
TMAZ 1	81	180	400	-110	30	120	378	4500	50	450	0.4	30
Nugget Zone	81	180	400	-120	30	120	378	4500	50	450	0.4	30

Table 3 Identification of matrerial parameters

In order to achieve a good convergence of the numerical analysis, material parameters are expressly chosen not to vary excessively from one area to another. The plasticity threshold is 180 MPa in the nugget zone, the weakest area, and 340 MPa in the base metal, the strongest one. There is a fast (b=400) negative non-linear isotropic hardening 1 (NLIH 1) in the joint that enables a strong reduction of the elastic domain of the metal. The second NLIH 2, which is slower than the first one, allows a slow cyclic hardening in the centre of the joint (visible on figure 16) and disappears in the base metal.

Different terms of non-linear kinematic hardenings (with backstresses X_1, X_2 and X_3) are used to correctly reproduce the evolution of hysteresis loops during cycles which parameters are not influenced by the microstructure. As mentioned here before, the dissolution of the precipitates in the nugget zone induces a soft behaviour (see figure 1) characterized by both a lower yield stress and a stronger reduction of the yield surface as plasticity evolves.

Single tension tests performed on welded specimens show finite strains, particularly in the nugget zone. It would be necessary to perform the simulations in a finite strain formalism to be coherent with this observation. However, despite the fact that this formalism induces longer computational times and more difficult numerical convergences, the final goal of this study is to be able to predict the fatigue crack initiation in welded panels. The fatigue cyclic load levels are much smaller (see figure 16 for example) and it is not necessary to refine the constitutive equations to reproduce as well as possible experimental results for large strains. However the formalism introduced in the Zset finite element program is able to deal with finite strain formalisms with corotational formulations [32, 33], but this option has not been considered in this project. More recent formalisms combining isotropic and kinematic hardenings in a finite strain framework are available in the literature [34, 35, 36, 37].

3.3 Connection between microstructure and mechanical parameters

The yield strength increment for each zone of the welded joint, including the elastic limit of the metal and the different nonlinear kinematic and isotropic hardenings, can be expressed as the sum of the precipitation strengthening ($\Delta\sigma_p$), the dislocation strengthening ($\Delta\sigma_{dis}$), the grain refinement strengthening ($\Delta\sigma_{H-P}$), the intrinsic yield strength of the metal (σ_l) and the solid solution elements ($\Delta\sigma_{ss}$):

$$\Delta\sigma_{exp}\left(\sigma_y + X + R\right) = \Delta\sigma_p + \Delta\sigma_{dis} + \Delta\sigma_{H-P} + \Delta\sigma_{ss} + \sigma_l$$

Firstly, the yield strength due to plates precipitates (T_1) can be evaluated with the equations proposed by Starink et al. [38] and Seidman et al. [39]

$$\Delta\sigma_{p,sh} = M\frac{\gamma_{apb}}{2\,b}\sqrt{\frac{3\,\pi^2\,\gamma_{apb}\,f_v\,\bar{r}}{32\,\Gamma}} \tag{1}$$

$$\Delta\sigma_{p,by} = 0.81\,M\frac{\gamma_{apb}}{2\,b}\sqrt{\frac{3\,\pi\,f_v}{8}} \tag{2}$$

The difference between equations 1 and 2 depends on the size of the precipitates. The Orowan mechanism states that precipitates are cut by dislocations if the mean radius of the precipitates is less than a critical radius, then equation 1 is used. If the mean radius of the precipitates is greater than this critical value, then the precipitates are bypassed by dislocations and equation 2 is used. The equations are composed by: M, the Taylor factor [39], γ_{apb}, the anti-phase boundary energy for precipitates [40], b, the Burgers vector [41], f_v, the volume fraction of precipitates in each zone of the joint, $\bar{r}$, the mean radius of the precipitates and Γ, the line tension of the dislocation [42]. This critical radius drives the transition between the shearing and bypassing mechanisms. It is obtained when equations 1 and 2 are equal. Then, the yield strength ($\Delta\sigma_p$) is obtained with:

$$\Delta\sigma_p = Min\left\{\Delta\sigma_{p,sh}, \Delta\sigma_{p,by}\right\}$$

Next, the contribution of the yield strength due to dislocation densities across the welded joint is calculated using the Taylor equation [40]:

$$\Delta\sigma_{dis} = M\,\alpha\,G\,b\,\rho^{1/2}$$

where α is the geometric factor of polycrystalline aluminium [42], G is the shear modulus of aluminium [41] and ρ is the dislocation density measured with X-ray spectrometry profiles. The values of dislocation densities used in this work are given by the work of Gao [13].
Thirdly, there is the contribution of the yield strength induced by the diminishing grain size in the material. This contribution is given by the Hall-Petch relation [43]:

$$\Delta\sigma_{H-P} = \frac{K}{\sqrt{D}}$$

where K is a material parameter to be adjusted and D is the average grain diameter in each area of the joint. The smaller the diameter, the greater the strength. Therefore, yield strength is estimated only in the area of the nugget zone where the microstructure is fully recrystallized.
Fourthly, the elements of the solid solution contribute to determine the yield strength in the joint. This contribution is determined by the Fleischer and Labusch equation [44-45].

$$\Delta\sigma_{ss} = \tau_c \exp\left(\frac{-k\,T}{E_0}\,2\,ln\left(\frac{\nu_0\,z}{V_0}\right)\right)$$

where τ_c is the critical shear stress of the polycrystalline aluminium [44], k and z are material parameters, T is the temperature, E is the modulus of elasticity, ν_0 is the jump frequency of a dislocation on a solid solution atom and V_0 is the initial dislocation velocity [45]. This contribution being too difficult to calculate, it is therefore estimated by an inverse technique knowing all the other contributions and the increment of the experimental yield strength.

Finally, the lattice stress σ_l is a constant parameter as proposed by Peierls-Nabarro [46-47] [13].
All the contributions are estimated and transcribed in table 4:

(MPa)	Base Metal	TAZ 2	TAZ 1	TMAZ 2	TMAZ 1	Nugget Zone
$\Delta\sigma_{\exp}$	488	488	448	428	398	388
$\Delta\sigma_p$	182	154	113	80	40	0
σ_l	30	30	30	30	30	30
$\Delta\sigma_{H-P}$	0	0	0	0	0	102
$\Delta\sigma_{dis}$	145	145	145	145	145	66
$\Delta\sigma_{ss}$	131	159	160	173	183	190

Table 4 Microstructure parameters in different zone of the joint

Parameters for T1 precipitates are not measured in the TMAZ1 and TMAZ2 zones, so a linearization of the precipitate contribution is performed between the TAZ and the Nugget zone.
There is a logical decay from the base metal, where precipitation plays an important role in the hardening of the material, to the nugget zone, where the precipitation is fully dissolved. The contribution of the yield strength due to grain refinement is calculated only for the equiaxed grains in the nugget zone, because the grains are very long in the other zones and the Hall-Petch relationship depends on their diameter.
Finally, the contribution of the yield strength of the solid solution elements increases slightly up to the centre of the joint. The value of this contribution is overestimated because many other types of precipitates are not taken into account. Nevertheless, the determination of these contributions to the material strength makes it possible to relate the mechanical parameters of the model to the evolution of the microstructure through the welded joint. These spatial evolutions allow to propose a constitutive model capable of reproducing the gradient of the mechanical properties and to take into account the effect of the microstructure in the different zones of the joint. This model is tested in the following section.

4. Finite element model validation

In a first step to validate the model, numerical simulations are carried out on a 3D sample with a perpendicular joint with respect to the loading direction. A first symmetry is carried out with the P1 plane to reduce the simulation time (figure 10). Moreover, the mechanical behaviour of the joint has only been identified for the forward side (AS), so the calculations consider a second symmetry with the P2 plane. However, the experimental results for the AS and the reverse side (RS) are compared with the simulations for each area of the welded joint.

The mesh used to calculate this sample is characterized by 23 511 nodes and 5 376 quadratic hexahedral and quadratic prismatic full integrated elements. A special procedure has been developed to introduce the evolution of the material parameters as a function of the position of the integration points in the structure in order to take into account the influence of the welded zone and to avoid strong discontinuities from one zone to another. This specific numerical procedure induced very stable calculations without convergence issues.

The anti-buckling device used during the experimental tests prevents the observation and analysis of the entire surface of the sample. Thus, only a useful area is chosen to compare experimental results (Figure 3).
First of all, the tensile test is simulated with imposed force loading. Results of the strain fields are presented for three different times corresponding to three different mechanical behaviours of the welded joint (figure 11). At 50 s during the tensile test, the mechanical behaviour of the structure remains elastic. At 75 s, the welded joint is barely deformed, whereas the nugget zone is already plastically deformed by almost 2%. And finally, at 98 s, at the maximum load of the tensile test, the nugget zone reaches a plastic strain of 11.5%.

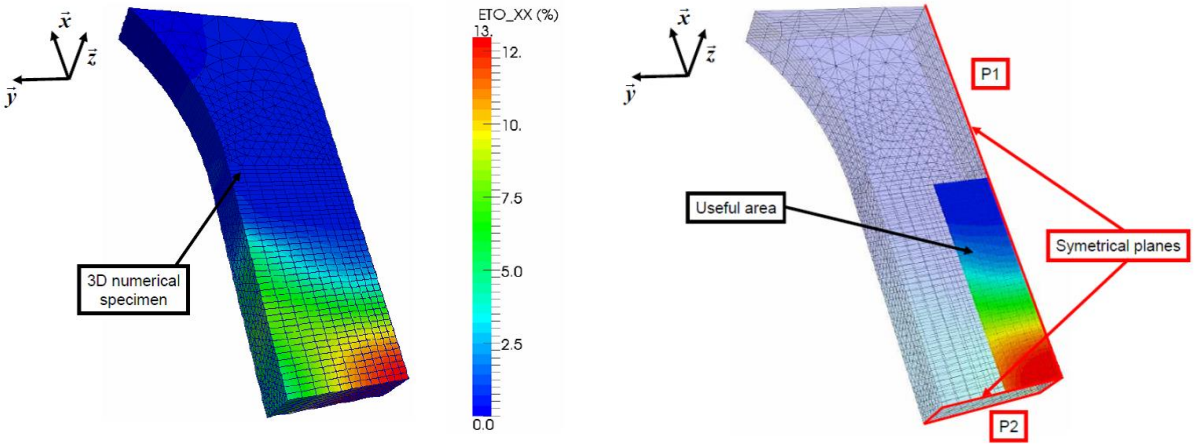

Fig 10 Meshed specimen with boundaries conditions and observed zone

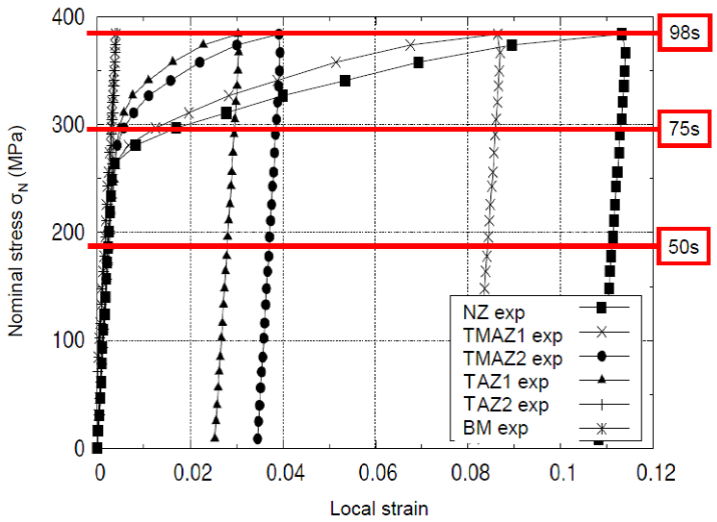

Fig 11 Stress-strain curves for different areas of the joint - Comparison of the results of the strain fields at three different times

Before analysing the results of the simulations, the local triaxiality has been calculated and enables to visualize the effects of the multiaxial stress state along the welded area. Results are presented in Figure 12. For a nominal stress of about 300 MPa, the sample surface presents a homogeneous triaxiality of about 0.3. This corresponds to a state of uniaxial stress in the different areas of the joint and confirms the choice of using the uniaxial nominal stress to identify the parameters of the constitutive equations. However, at the end of the test and in the TAZ, the triaxiality increases and the mechanical behaviour reaches a multi-axial state. In order to improve the mechanical model, the parameters must be identified again by considering the stresses in the three directions.

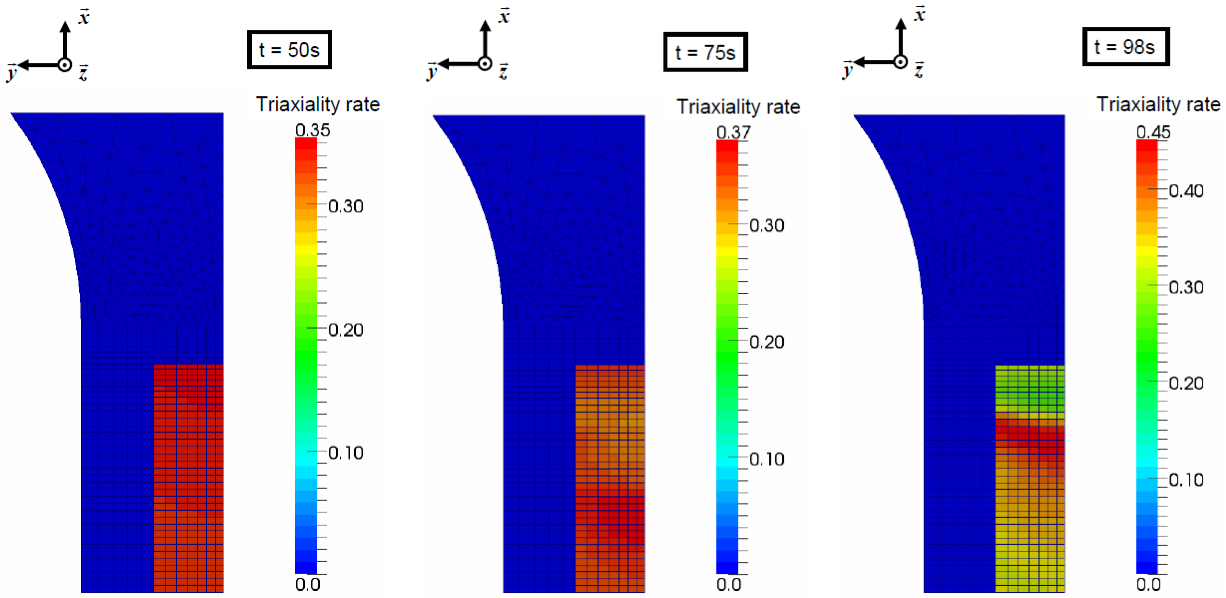

Fig 12 Triaxiality stress calculated on the useful zone of the specimen

Figure 13 shows a comparison of strain fields obtained experimentally with the DIC method and by the finite element calculation for the single tension test. The strain gradient is similar in both cases and the contours at 1% and 1.5% of deformation allow to distinguish a similar evolution of the deformation gradient between the nugget zone and the base metal.

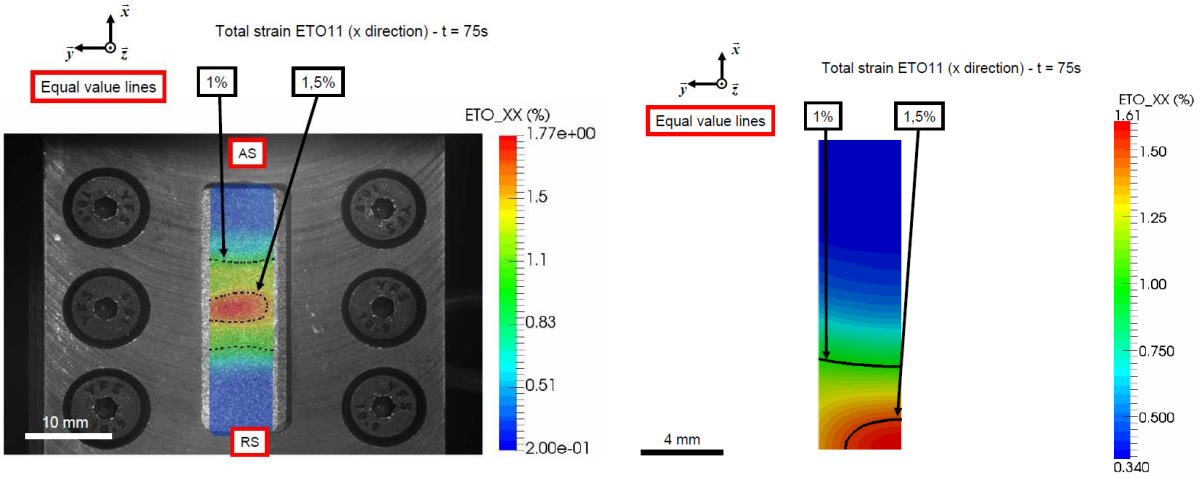

Fig 13 Comparison of strain fields for a single tension test. Experimental (left) and numerical (right) results at 75s

After this first validation, the strain fields can also be compared for a cyclic test. An example is shown in Figure 14 when the welded structure is loaded at the maximum compressive load. The nominal stress is approximately -300 MPa. The strain fields plotted for an overall strain of -0.5% and 0.1% allow defining two distinct zones. The first one gathers the maximum plastic strain in the nugget zone. The second one is located in the Thermal-affected zone with a maximum of the compressive strain about -0.7%. Results of the simulation show that this model is capable of reproducing the gradients of the mechanical behaviour of the joint even if the maximum strain levels don't match exactly the experimental results.

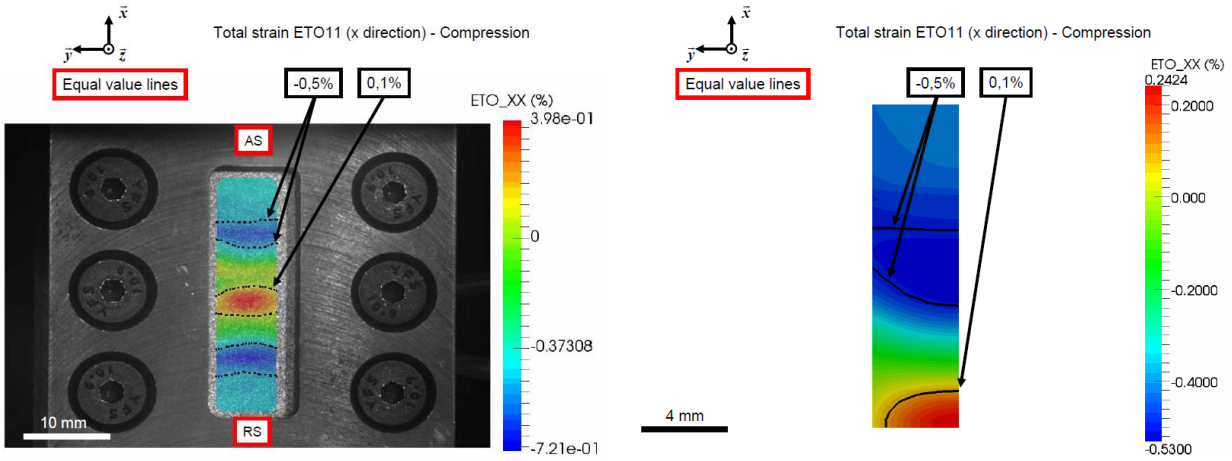

Fig 14 Comparison of strain fields for a cyclic test. Experimental (left) and numerical (right) results at 75s (compression load)

Another way to verify the accuracy of the model with respect to experimental results is to analyze the local strain - nominal stress curves in different areas of the welded joint. The nugget zone, where strains are maximum (figure 15 on the left), and the TAZ1 zone, located far from the centre of the joint and therefore with less plastic strains (figure 15 on the right), are presented and compared in the different rolling directions of the material (T, L and D). The comparisons show no big differences between them up to a strain of about 7%, corresponding to a nominal stress of about 350 MPa, for the nugget zone (Figure 15 left). The isotropic criterion is adequate for this zone but does not allow to reproduce the maximum strain difference observed between the three directions L, T and D. These curves explain the difference in strain levels observed between the experimental and numerical strain fields (Figure 13).

Within the TAZ1 zone, a significant difference appears for a nominal stress of about 300 MPa (Figure 15 on the right). Moving from the nugget zone, where the microstructure is fully recrystallized, to the base metal, which is strongly anisotropic, the assumption of an isotropic model is partially correct. For the analysis of the welded joint loaded in fatigue, a maximum plastic deformation of about 2% will be applied in the nugget zone. Thus, in this case, the identified isotropic model will be appropriate.

For higher deformations, the limits of this model, as perceived through the tensile test, show a material too stiff for the TAZ1 zone..

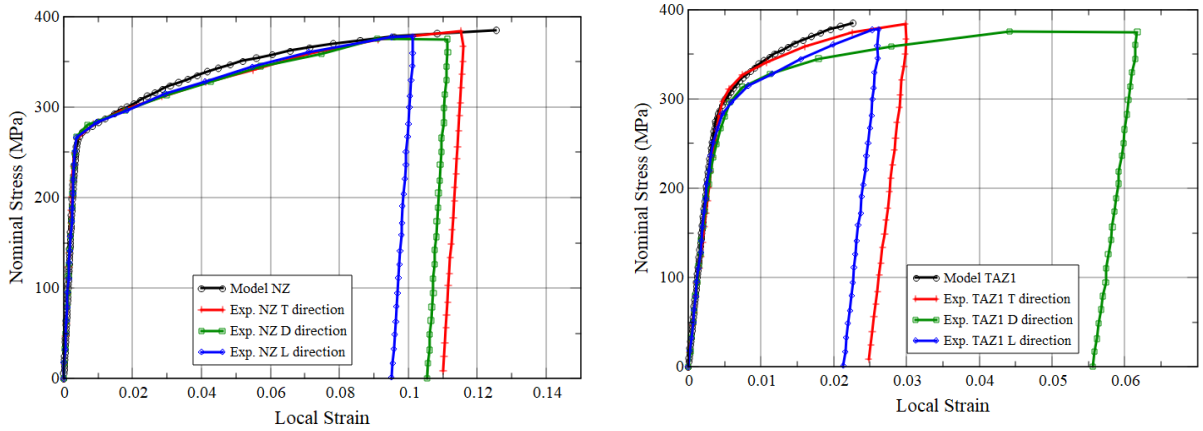

Fig 15 Nugget Point (Left) and TAZ1 Point (Right)

Hereinafter, the cyclic test is simulated with a symmetrical load and 4 different load levels. The cyclic loading applied on each level allows the investigation of the isotropic hardening of the material. For the sake of clarity only the first and last cycle of each load level are plotted in these figures.

As it has been detailed before, the constitutive equations consist of three terms of non-linear kinematic hardening which allow a good representation of the hysteresis loops of the cycles. The first stress level in the nugget area (Figure 16) shows the possible effects of the anti-buckling device on the structure with a relatively poor representation of the material behaviour in compression. This device prevents the behaviour of the nugget area from

reaching the minimum strain imposed experimentally in compression. Nevertheless, the difference in the plastic strain obtained during the unloading path is approximately the same experimentally and numerically.
Another effect observed in the experimental result, but not reproduced numerically, is the change in the Young's modulus during the cyclic loading, which is more noticeable in the TAZ1 zone at the fourth stress level (Figure 17).
The 2 non-linear isotropic hardenings used in the model reproduce correctly the closure of the loops for the first level. This allows to obtain the correct strains for the three following levels.
Numerically, a saturation of the hardening is observed after about 30 cycles in the first level. Experimentally, a new hardening, of small amplitude, is observed for the other levels (see Figure 6), however, the model is already saturated and cannot reproduce this effect.

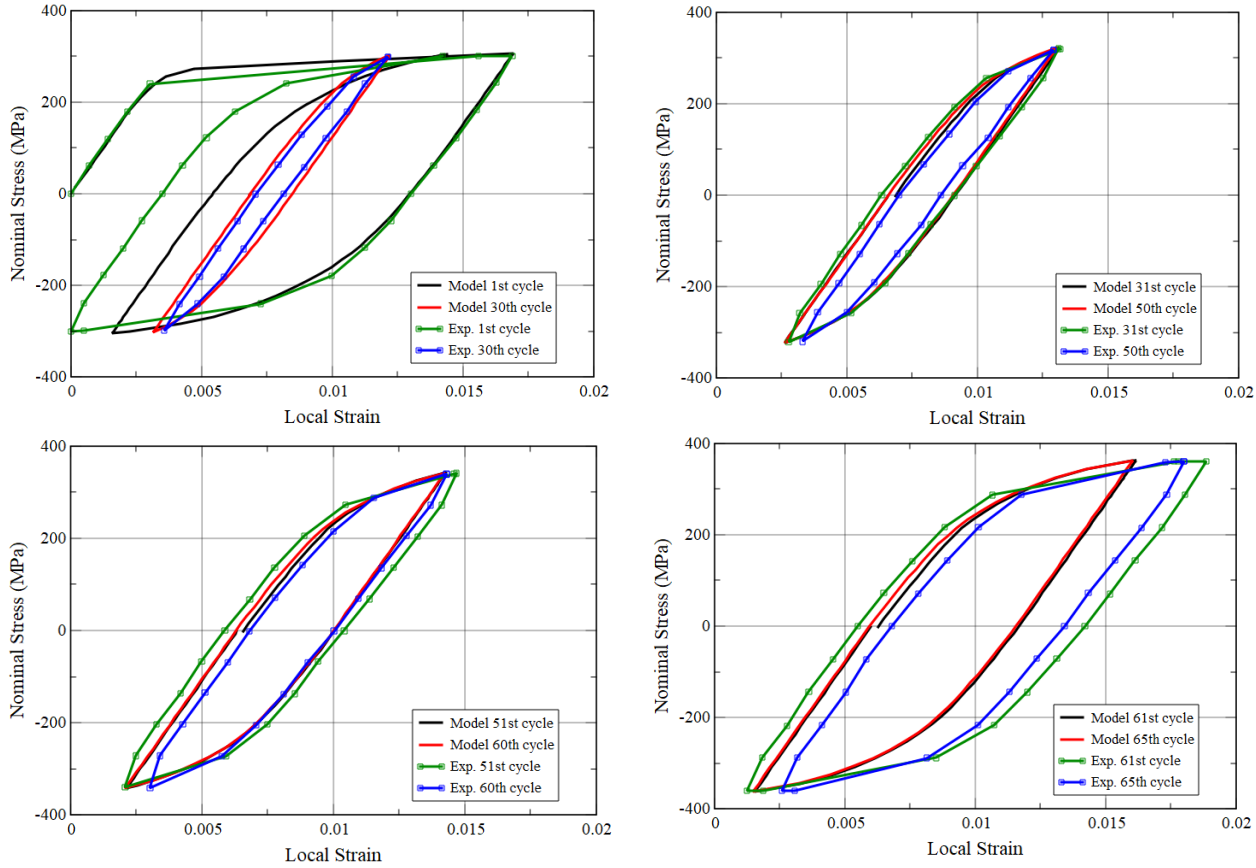

Fig 16 Hysteresis loops in the nugget Zone

Finally, the hysteresis loops are less open in the TAZ1 zone (Figure 17) than in the Nugget one where the strains are higher. As for the tensile test, the maximum strain concentrations are located in the Nugget Zone. This fact forces the TAZ1 zone to remain in a quasi-elastic state with very slightly open loops, making more difficult the identification of the mechanical parameters of the model. Improvements can be achieved to reproduce the full mechanical behaviour of the different zones of the joint. The first one would be to take into account the anisotropic behaviour of the thermal affected area and the base metal.

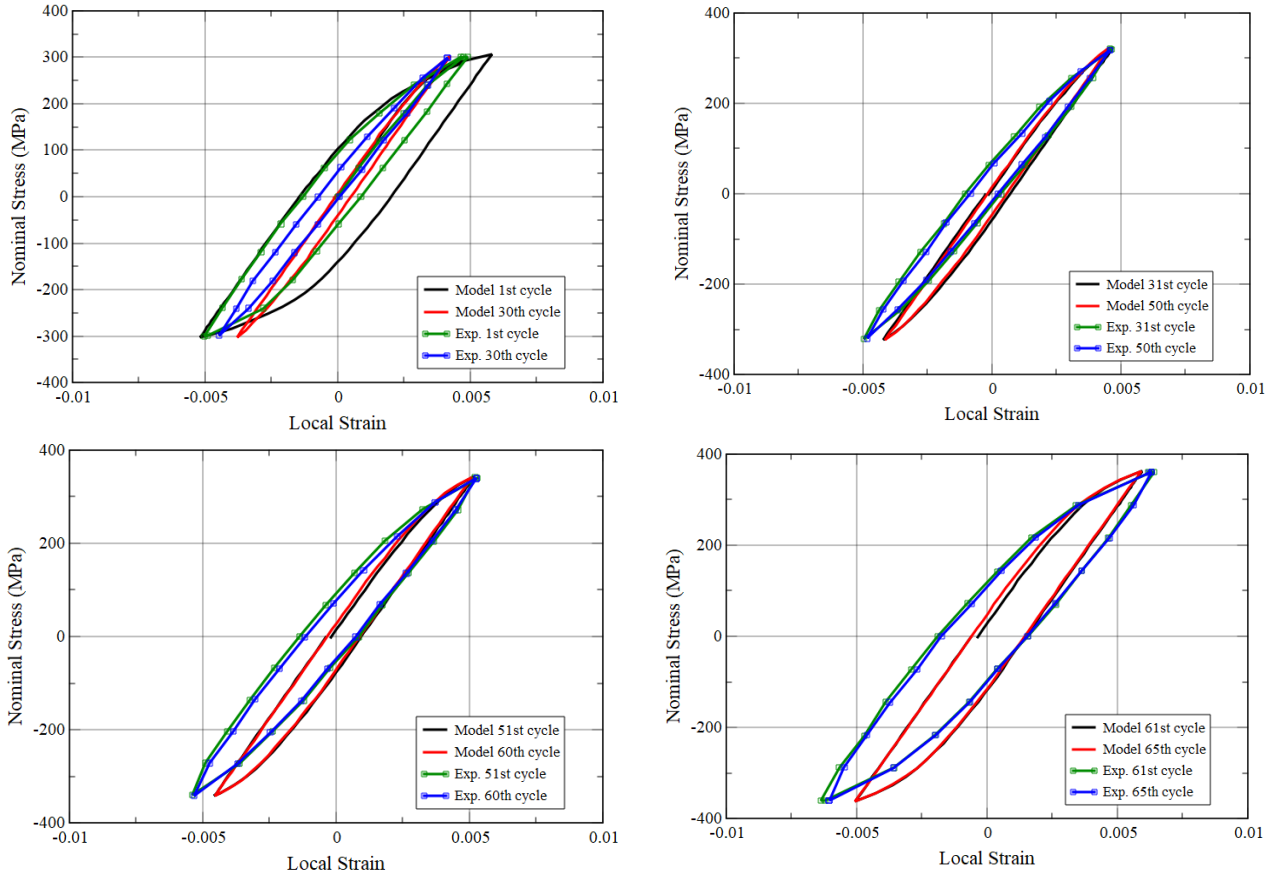

Fig 17 Hysteresis loops in the Thermal Affected Zone

Another difficulty arising during the identification and validation process of the constitutive equations relies in the flat hardening appearing close to the saturation. This particular situation may induce a large discrepancy on the strain levels for a small stress perturbation as it can be observed in figure 16 for the first cycle in compression or the 60th cycle in tension. Despite these difficulties, the results obtained with the proposed model, varying the material parameters along the different welded zones, are quite accurate.

5. Conclusion

This study is concerned with the cyclic mechanical characterization and modelling of 2198-T8 sheets welded by the FSW process. Microstructural analysis of the welded joints, combined with hardness measurements taken across the joint, showed significant changes in the microstructure resulting from this process. Transverse specimens 3.18 mm thick were machined from the welds and mechanically tested with the weld direction perpendicular to the loading direction. Tensile and cyclic tests were carried out at room temperature. Analysis of the results obtained by DIC confirmed that this technique is capable of providing the displacement field along the entire length of the welded joint and thus allows the calculation of the strain field. Based on these experimental results, an initially isotropic constitutive model of the welded joint was proposed and identified. The 3D finite element simulations of more complex loads have shown that this formalism is not sufficient to reproduce the mechanical behaviour of all the zones of the welded joint under multi-axial conditions. Next steps, already in progress [48], are as follows:

- propose more complex constitutive equations in order to reproduce both the isotropic behaviour of the nugget zone and the anisotropic behaviour of the base metal and the other zones of the structure.
- simulate the cyclic behaviour of welded structures (real components or complex biaxial specimens) with the new constitutive equations
- analyse the impact of the friction stir welding process on the crack initiation and propagation

Acknowledgements

The authors would like to acknowledge Constellium for providing aluminium sheet metal.

References

1. W. Thomas. www.twi-global.com. TWI – 1991.
2. R. S. Mishra, M. W. Mahoney, Friction Stir Welding and Processing. Chapter 5: 71-110 – 2007.
3. N. D. Alexopoulos, E. Migklis, A. Stylianos, D. P. Myriounis, Fatigue behavior of the aeronautical Al-Li (2198) aluminum alloy under constant amplitude loading, International Journal of Fatigue, Volume 56: 95-105 – 2013.
4. T. Le Jolu, Influence des défauts de soudage sur le comportement plastique et la durée de vie en fatigue de soudures par friction-malaxage d'un alliage Al-Cu-Li, Thèse de doctorat, Mines ParisTech – 2011.
5. Y. Demmouche, Étude du comportement en fatigue d'assemblages soudés par FSW pour applications aéronautiques, PhD Arts et Métiers ParisTech – 2012.
6. W. D. Lockwood, B. Tomaz, A. P. Reynolds, Mechanical response of friction stir welded AA2024 : experiment and modeling, Materials Science and Engineering A, Volume 323: 348-353 – 2002.
7. A. P. Reynolds, F. Duvall, DIC for determination of weld and base metal constitutive behaviour, Department of Mechanical Engineering, University of South Carolina, Columbia S.C. – 1999.
8. B. A. McWilliams, J. H. Yu, C. F. Yen, Numerical simulation and experimental characterization of friction stir welding on thick aluminium alloy AA2139-T8 plates, Materials Science and Engineering, Volume 585: 243-252 – 2013.
9. C. Leitao, I. Galvao, R.M. Leal, D.M. Rodrigues, Determination of local constitutive properties of aluminium friction stir welds using digital image correlation, Materials and Design, Volume 33: 69-74 – 2012.
10. C. Gallais, Joints soudés par friction malaxage d'alliages d'aluminium de la série 6xxx : caractérisation et modélisation, PhD Université de Grenoble – 2005.
11. T. Dorin, Mécanismes de durcissement structural par des précipités anisotropes dans un alliage Al-Cu-Li de troisième génération, PhD Université de Grenoble – 2013.
12. P. Cavaliere, M. Cabibbo, F. Panella, A. Squillace, 2198 Al–Li plates joined by Friction Stir Welding: Mechanical and Microstructural Behavior, Mater. And Design 30: 3622-3631 – 2009.
13. C. Gao, Z. Zhu, J. Han, H. Li, Materials Science and Engineering A, Volume 639: 489-499 – 2015.
14. K. Krasnowski, C. Hamilton, S. Dymek, Influence of the tool shape and weld configuration on microstructure and mechanical properties of the Al 6082 alloy FSW joints, Archives of civil and mechanical engineering, Volume 15: 133 – 141 – 2015.
15. H. K. Hardy, J. M. Silcock, The phase sections at 500 and 350°C of Al rich Al-Cu-Li alloys, Journal of the Institute of Metals, Volume 84: 423-428 – 1955.
16. A. Steuwer, M. Dumont, J. Altenkirch, S. Birosca, A. Deschamps, P.B. Prangnell, P.J. Withers, A combined approach to microstructure mapping of an Al-Li AA2199 friction stir weld, Acta Mater. 59: 3002-3011 – 2011.
17. F.W. Gayle, F.H. Heubaum, J.R. Pickens, Structure and properties during aging of an ultra-high strength aluminum-copper-lithium-silver-magnesium alloy, Scr. Metall. And Mater. 24: 79-84 – 1990.
18. P. Donnadieu,Y. Shao, F. De Geuser, G.A. Botton, S. Lazar, M. Cheynet, M. de Boissieu, A. Deschamps, Atomic structure of T1 precipitates in Al-Li-Cu alloys revisited with HAADF-STEM imaging and small-angle X-ray scattering, Acta Mater. 59: 462–472 – 2011.
19. A. Deschamps, B. Decreus, F. De Geuser, T. Dorin, M. Weyland, The influence of precipitation on plastic deformation of Al-Cu-Li alloys, Acta Mater. 61: 4010–4021 – 2013.
20. B. Decreus, A. Deschamps, F. De Geuser, P. Donnadieu, C. Sigli, M. Weyland, The influence of Cu/Li ratio on precipitation in Al–Cu–Li–x alloys, Acta Materialia, Volume 61: 2207-2218 – 2013.
21. S. Zhang, W.D. Zeng, W.H. Yang, C.L. Shi, H.J. Wang, Ageing response of a Al–Cu–Li 2198 alloy, Mater. & Design 63: 368-374 – 2014.
22. C. Gao, Y. Ma, L-Z. Tang, P. Wang, X. Zhang, Microstructural evolution and mechanical behavior of friction spot welded 2198-T8 Al-Li alloy during aging treatment, Mater. & Design 115: 224–230 – 2017.
23. Schindelin, J.; Arganda-Carreras, I. & Frise, E. et al., "Fiji: an open-source platform for biological-image analysis", Nature methods 9(7): 676-682 – 2012.
24. B. Decreus, Etude de la précipitation dans les alliages Al-Li-Cu de troisième génération : relations entre microstructures et propriétés mécaniques, PhD Université de Grenoble – 2010.
25. G.K. Williamson, W.H. Hall, X-ray line broadening from filed aluminium and wolfram, Acta Mell. 1: 22-31 – 1953.
26. S. Khan, O. Kintzel, J. Mosler, Experimental and numerical lifetime assessment of Al 2024 sheet, International Journal of Fatigue, Volume 37: 112-122 – 2011.

27. ARAMIS Software. www.gom.com.
28. J. Chen, Ductile Tearing of AA2198 Aluminum-Lithium Sheets for Aeronautic Application, Thèse de doctorat, Mines ParisTech – 2011.
29. J. Lemaitre, J.L. Chaboche, Mechanics of Solid Materials, Cambridge University Press – 1994.
30. J. Besson, G. Cailletaud, J.L. Chaboche, S. Forest, Non-Linear Mechanics of Materials, Springer Sci. – 2009.
31. H. Altenbach, A. Bolchoun, V. Kolupaev, A. Phenomenological yield and failure criteria. In: Plasticity of pressure-sensitive materials. Springer, Berlin, S. Heidelberg, 49-152 - 2014.
32. A.E. Green and P.M. Naghdi, A General Theory of Elastic-Plastic Continuum, Arch. Rat. Mech. Anal. 18 : 251-281, 1965.
33. J.C. Nagtegaal, On the Implementation of Inelastic Constitutive Equations with Special Reference to Large Deformation Problems, Comp. Meth. Applied Mech. Eng., 33, 469-484 - 1982.
34. A. Lion, Constitutive modelling in finite thermoviscoplasticity: a physical approach based on nonlinear rheological elements, International Journal of Plasticity, 16, 469-494 - 2000.
35. A. V. Shutov, R. Kreißig, Finite strain viscoplasticity with nonlinear kinematic hardening: Phenomenological modeling and time integration, Computer Methods in Applied Mechanics and Engineering, 197., Nr. 21-24, 2015-2029 - 2008.
36. I.N. Vladimirov, M.P. Pietryga, S. Reese, Anisotropic finite elastoplasticity with nonlinear kinematic and isotropic hardening and application to sheet metal forming. International Journal of Plasticity, 26. Jg., Nr. 5, S. 659-687 - 2010.
37. A. V. Shutov, Models of nonlinear kinematic hardening based on different versions of the rate-independent Maxwell fluid, In: COMPLAS XIV: proceedings of the XIV International Conference on Computational Plasticity: fundamentals and applications. CIMNE, 385-396 - 2017.
38. M. Starink, P. Wang, I. Sinclair, P. Gregson, Microstructure and strengthening of Al-Li-Cu-Mg alloys and MMCs: II. Modelling of yield strength, Acta Materiala, Volume 47: 3855-3868 – 1999.
39. D.N. Seidman, E.A. Marquis, D.C. Dunand, Precipitation strengthening at ambient and elevated temperatures oh heat-treatable Al(Sc) alloys, Acta Metallurgica, Volume 50: 4021-4035 – 2002.
40. N. Hansen, Boundary strengthening over five length scales, Advanced Engineering Materials, Volume 7: 815-821 – 2005.
41. W. Woo, L. Balogh, T. Ungár, H. Choo, Z. Feng, Grain structure and dislocation density measurements in a friction-stir welded aluminium alloy using X-ray peak profile analysis, Materials Science and Engineering A, Volume 498: 308-313 – 2008.
42. J. Huang, A. Ardell, Strengthening mechanisms associated with T1 particles in 2 Al-Li-Cu alloys, Journal of Physics, Volume 48: 373-383 – 1987.
43. R. W. Armstrong, Past to Present Nanoscale Connections, Mater Trans 55: 2–12 – 1987.
44. R. L. Fleisgher, Solution hardening, Acta Metallurgica, Volume 9: 996-1000 – 1961.
45. R. Labusch, A statistical theory of solid solution hardening, Physica Status Solidi B, Volume 41: 659-669 – 1970.
46. R. Peierls, The size of a dislocation, Proceedings of the Physical Society, Volume 52: 34-37 - 1940.
47. F. R. N. Nabarro, Dislocations in a simple cubic lattice, Proceedings of Physical Society, Volume 59: 256-272 – 1947.
48. X. Truant, Etude et modélisation du comportement mécanique de panneaux de structure soudés par friction-malaxage (FSW), PhD Ecole des Mines de Paris – 2018.